

# Supporting Information

## Extremely efficient photocurrent generation in carbon nanotube photodiodes enabled by axial electric field

Daniel R. McCulley<sup>1</sup>, Mitchell J. Senger<sup>1</sup>, Andrea Bertoni<sup>2</sup>, Vasili Perebeinos<sup>3</sup>, Ethan D. Minot<sup>1\*</sup>

<sup>1</sup>*Department of Physics, Oregon State University, Corvallis, Oregon 97331, USA*

<sup>2</sup>*Istituto Nanoscienze-CNR, Via Campi 213a, I-41125 Modena, Italy*

<sup>3</sup>*Department of Electrical Engineering, University of Buffalo, The State University of New York, Buffalo, NY 14260, USA*

*\*Ethan.Minot@oregonstate.edu*

### Contents

1. Optical interference from back reflection
2. Optical power density of the incident laser beam
3. Average spectral shift and calculated Stark shift
4. Calculation of carbon nanotube oscillator strength
5. Spectral width of exciton peaks
6. Self-consistent field calculations
7. Imaging the intrinsic region length
8. Intrinsic region length determined from electrostatic modeling
9. Cross-check of calculated charge density
10. Cross check for photo-conductance
11. Nanotube growth
12. Extended data for Devices A to J

## 1. Optical interference from back reflection

We used a finite difference time domain (FDTD) simulation to determine the enhancement of optical power caused by back reflection from the split-gate electrodes. Inputs to the simulation included the device geometry, the dielectric functions of the device materials (platinum and silicon oxide) and the profile of the incident light beam. The beam profile was either a focused or defocused Gaussian beam profile coming from a numerical aperture that matches the microscope objective used in our experiment. We determined the optical power at a position corresponding to the center of the suspended carbon nanotube (CNT). The exact height of the nanotube could be 650 nm above the split gates (i.e. level with the top of the source and drain electrodes as shown in Fig. S1a) or slightly less than 650 nm if the CNT adheres to the side wall of the source or drain electrode (Fig. S1b). We achieved the best match between simulations and experiments when we assumed the CNT height is 617 nm above the split gates.

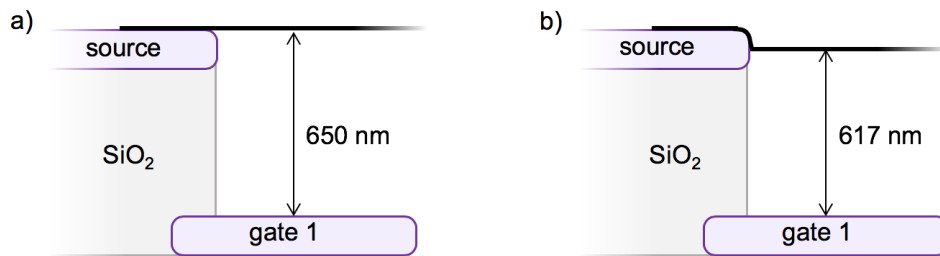


**Figure S1. a)** Cross sectional diagram of a CNT grown flat across the surface of the electrodes. **b)** Cross sectional diagram of a CNT that has adhered to the side of the electrode before crossing the trench.

Figure S2a shows the boundary of the FDTD simulation as well as the Gaussian profile of a plane wave propagated through a 50X objective with a numerical aperture of 0.55. Figure S2b shows the interference strength  $\beta$  (the enhancement of the incident power due to back reflection) when the incident wavelength is 1630 nm. Figure S2c shows  $\beta$  at the center of the CNT when the incident light is either a focused beam and defocused beam. We also plot the ratio,  $\beta_{\text{def}}/\beta_{\text{foc}}$ , which we discuss in the next section. Due to uncertainty in the exact height of the CNT, there is uncertainty in  $\beta$ . Figure S2d shows the effect of changing the CNT height by  $\pm 17$  nm.

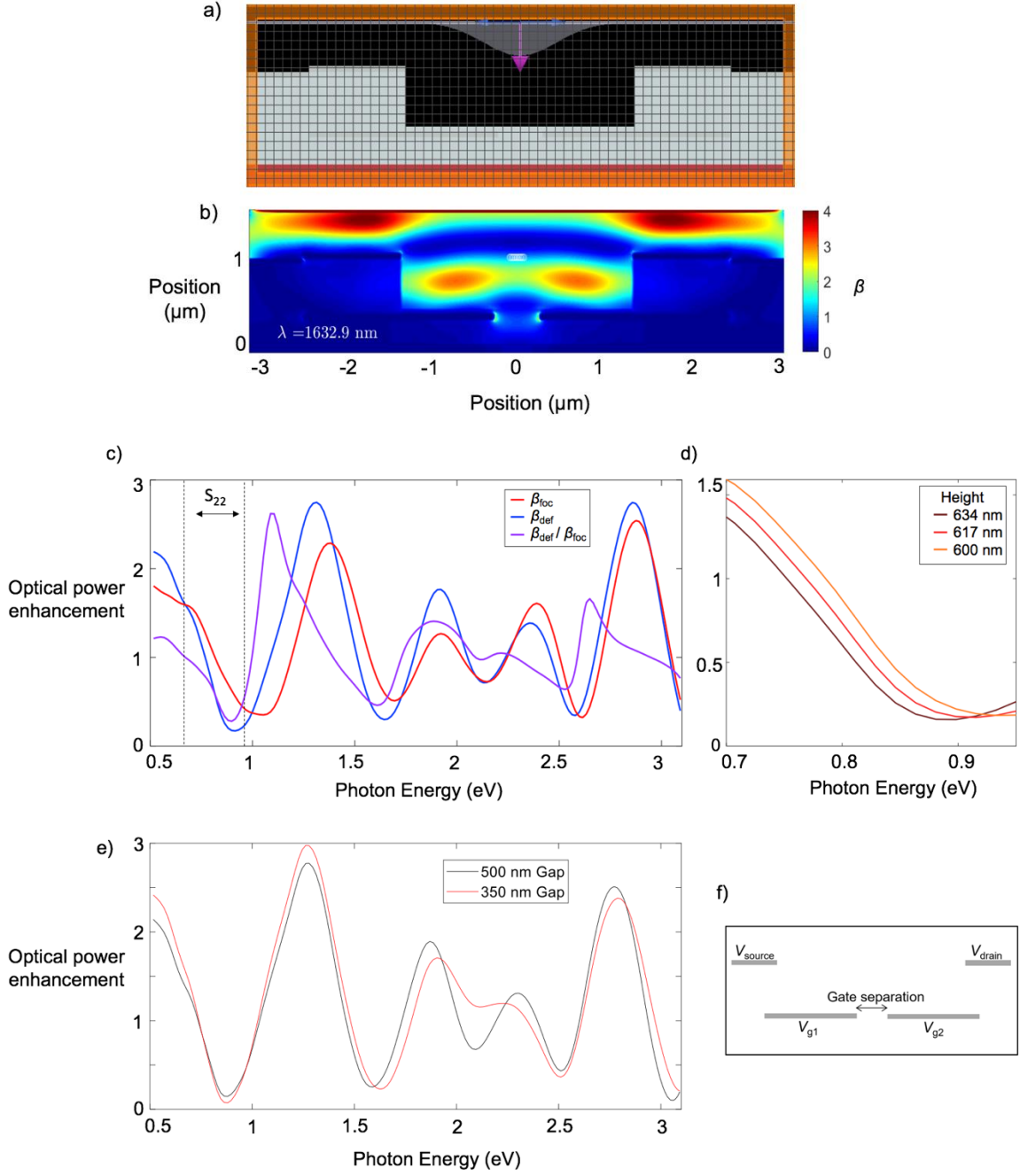


**Figure S2.** **a)** The FDTD simulation window with a focused Gaussian beam profile incident on the electrode geometry. **b)** The optical interference strength,  $\beta$ , at a wavelength of 1630 nm. **c)** Interference strength vs. photon energy measured at the center of the CNT, 616 nm above the top surface of the split gate electrodes. The range of  $S_{22}$  peak energies for the eight CNTs discussed in the main text is indicated. **d)** The interference strength vs. photon energy at different heights above the top surface of the split gate electrodes. **e)** The change in interference strength (defocused beam, height 616 nm) when the separation distance between the split-gates is reduced from 500 nm to 350 nm. **f)** Cross-sectional diagram of the electrode layout showing the separation between the gates.

The optical interference strength is affected by the separation distance between the split-gate electrodes (Fig. S2e). The effect is most prominent when the wavelength is similar to the size of the gap. The nominal gap size (from the photolithography mask) is 500 nm, but SEM characterization shows that the gap can be as small as 350 nm. Figure S2e shows the effect of changing the gap from 500 nm to 350 nm. The spectrum is most affected in the range 1.5 – 2.5 eV. For measurements in the spectral range of the  $S_{22}$  resonance, the uncertainty in  $\beta$  due to the gap size is negligible.

## 2. Optical power density in the incident laser beam

In the main text we describe the relationship

$$\Phi = \frac{P_0 \cdot \beta}{\hbar\omega \cdot A_{\text{spot}}}, \quad (\text{S1})$$

where  $P_0$  is the laser power and  $A_{\text{spot}}$  is the effective area of the laser point spread function (PSF). After determining  $\beta$ , the remaining challenge is to find  $A_{\text{spot}}$ .

The effective area of the PSF for the focused laser spot,  $A_{\text{spot,foc}}$ , can be found from the scanning photocurrent image (Fig. S3b). Because the intrinsic region of the CNT photodiode is much smaller than the laser spot, the photocurrent image samples the PSF. The spot area is found by integrating the PSF

$$A_{\text{spot}} = \int PSF(x, y) dx dy \quad (\text{S2})$$

where  $PSF(0,0) = 1$ . The integral of Eq. S2 is calculated by fitting Gaussians to the experimental data. For the simplest PSF,  $A_{\text{spot}}$  can be calculated from a single Gaussian fit where

$$A_{\text{spot}} = \int \exp\left(\frac{-x^2}{a^2}\right) \cdot \exp\left(\frac{-y^2}{b^2}\right) dx dy = \pi ab. \quad (\text{S3})$$

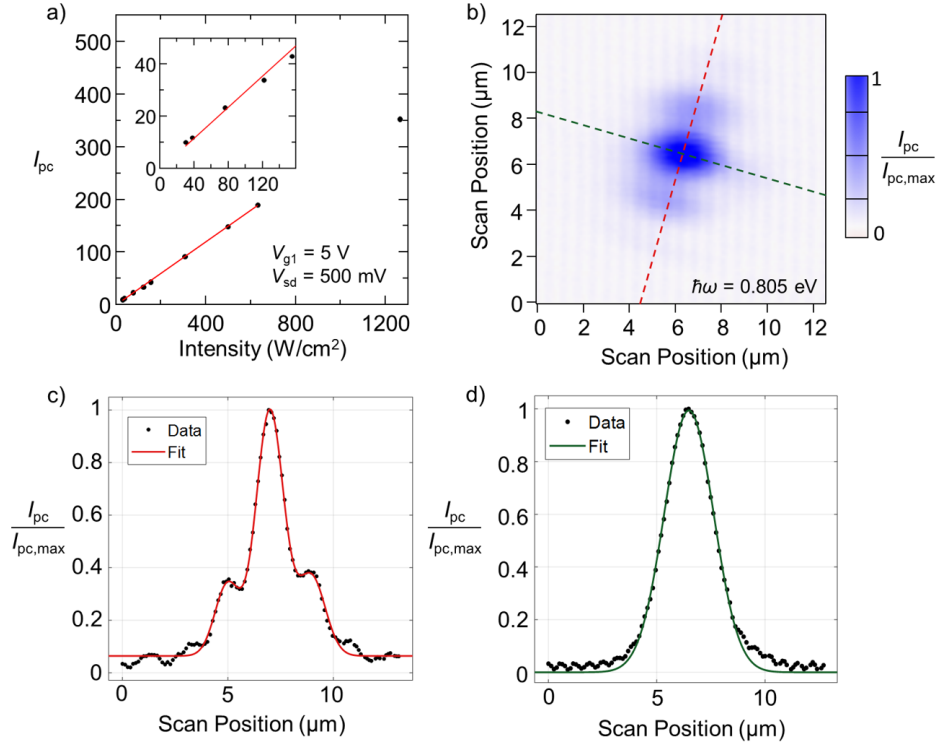


**Figure S3. a)** The typical photocurrent response as a function of laser intensity. The red linear fit has a slope of  $0.3 \text{ pA cm}^2 \text{ W}^{-1}$ . **b)** A scanning photocurrent image sampling the PSF of the laser spot. **c)** Cross section of the photocurrent image in b) along the dashed red line along with a fit using the sum of three Gaussians (fit parameters in Device A summary below). **d)** Cross section of the photocurrent image in b) along the dashed green line along with a Gaussian fit (fit parameters in Device A summary below).

The photocurrent spot in Fig. S3b has a more complicated PSF. To fit the PSF in Figure S3b, we used a single Gaussian along one axis (Fig. S3d) and three Gaussians along the other (Fig. S3c). The spot area is then given by

$$\begin{aligned}
 A_{\text{spot}} &= \int \exp\left(\frac{-y^2}{w_y^2}\right) \cdot \left( a_{x,0} \cdot \exp\left(\frac{-(x-x_0)^2}{w_{x,0}^2}\right) + a_{x,1} \cdot \exp\left(\frac{-(x-x_1)^2}{w_{x,1}^2}\right) + a_{x,-1} \cdot \exp\left(\frac{-(x-x_{-1})^2}{w_{x,-1}^2}\right) \right) dx \\
 &= \pi w_{y,0} (a_{x,0} w_{x,0} + a_{x,1} w_{x,1} + a_{x,-1} w_{x,-1}). \quad (\text{S4})
 \end{aligned}$$

For the image in Fig. 3b we found  $A_{\text{spot}} = 6.7 \text{ } \mu\text{m}^2$  (see Device A summary for the fit parameters).

Our protocol for measuring a photocurrent spectrum used a defocused laser such that  $A_{\text{spot}} > 100 \text{ } \mu\text{m}^2$ . For these large spot areas, photocurrent imaging was not feasible and we used a different approach to find  $A_{\text{spot}}$ . We rely on the linear relationship between photocurrent and

intensity (Fig. S3a). The linear response of the photocurrent signal implies that the ratio of photocurrent to photon flux remains constant, which is given by

$$\frac{I_{pc,foc}}{\Phi_{foc}} = \frac{I_{pc,def}}{\Phi_{def}}, \quad (S5)$$

where  $I_{pc,foc}$  and  $I_{pc,def}$  are the focused and defocused photocurrent respectively. Combining Eq. S1 and S5 we find that the area of the defocused spot can be calculated from

$$A_{spot,def} = \left( \frac{\beta_{def} \cdot P_{0,def}}{\beta_{foc} \cdot P_{0,foc}} \right) \cdot \left( \frac{I_{pc,foc}}{I_{pc,def}} \right) \cdot A_{spot,foc} \quad (S6)$$

where  $P_{foc}/P_{def}$  is the ratio of laser powers for focused and defocused light, and  $\beta_{foc}/\beta_{def}$  is the ratio of enhancement factors for focused and defocused light.

### 3. Average spectral shift and calculated Stark shift

We propose that the observed spectral shifts of exciton resonances are caused by two independent mechanisms. The first mechanism is the axial strain that is generated by the electrostatic force pulling down on the CNT. The second mechanism is the Stark shift.

Given a large sample of CNTs, the average spectral shift caused by axial strain should be zero. CNTs with  $(n - m) \bmod 3 = 1$  will exhibit strain-induced redshift, while an equal number of CNTs with  $(n - m) \bmod 3 = 2$  will exhibit strain-induced blueshift. Using our experimental data (Fig. 4a of main text) we calculated the average spectral shift of all eight CNTs. The  $(n - m) \bmod 3 = 2$  family of CNT was weighted more heavily, because only 2 out of 8 CNTs were from this family. The weighted average (Fig. S4) shows a clear trend toward redshift.

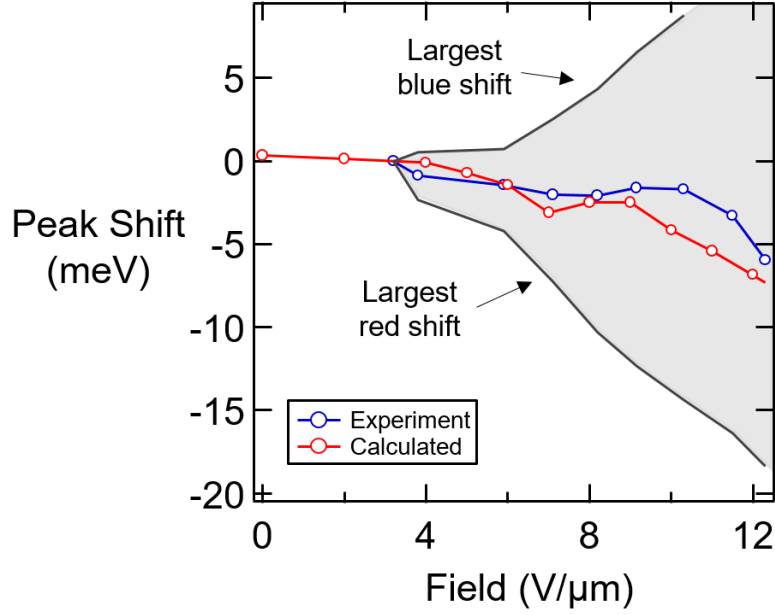


**Figure S4.** The blue curve shows the weighted average of the  $S_{22}$  peak shift for the eight CNTs discussed in the main text. The red curve shows the calculated average Stark shift of the  $S_{22}$  resonance for the same eight CNTs. The grey boundaries show the spread of peak shifts observed in the experiment.

In Fig. S4, we compare the weighted average from experimental data (blue line) with the predicted average Stark shift the same eight chiralities (red line). There is good agreement between theory and the observed average shift. This agreement supports our proposed interpretation that strain causes most of the observed peak shift, but the Stark effect causes a small but noticeable shift towards lower energies.

#### 4. Calculation of carbon nanotube oscillator strength

The oscillator strength of an exciton resonance in a CNT with a specific chiral index is calculated using the equation<sup>1</sup>

$$\int_{S_{ii}} \sigma_c d(\hbar\omega) = \frac{45.9}{(p + 7.5)D} \times 10^{-18} \text{eV} \cdot \text{cm}^2, \quad (\text{S7})$$

where  $D$  is the nanotube diameter and  $p$  is an integer indexing the optical transitions of both semiconducting and metallic nanotubes ( $p = 2$  for  $S_{22}$  and  $p = 4$  for  $S_{33}$ ). The atoms per length in the nanotube,  $N_L$ , is given by

$$N_L = \frac{4(n^2 + m^2 + 2nm)}{\sqrt{3}a_c}, \quad (\text{S8})$$

where  $(n, m)$  are the chiral indices of the CNT and  $a_c = 0.14$  nm is the carbon-carbon bond length. The absorption cross section per atom,  $\sigma_c$ , can be multiplied by  $N_L$  to find an effective absorptive width of the nanotube.

To verify that Eq. S7 is valid at large  $F$ , we calculated the expected absorption cross-section spectrum as a function of  $F$ . For this calculation, we used the Bethe-Salpeter equation for an exciton in the presence of a static axial electric field similar to the methods used by Perebeinos and Avouris in 2007.<sup>2</sup> Figure S5b shows that the oscillator strength decreases by only ~5% at the highest fields used in our experiments.

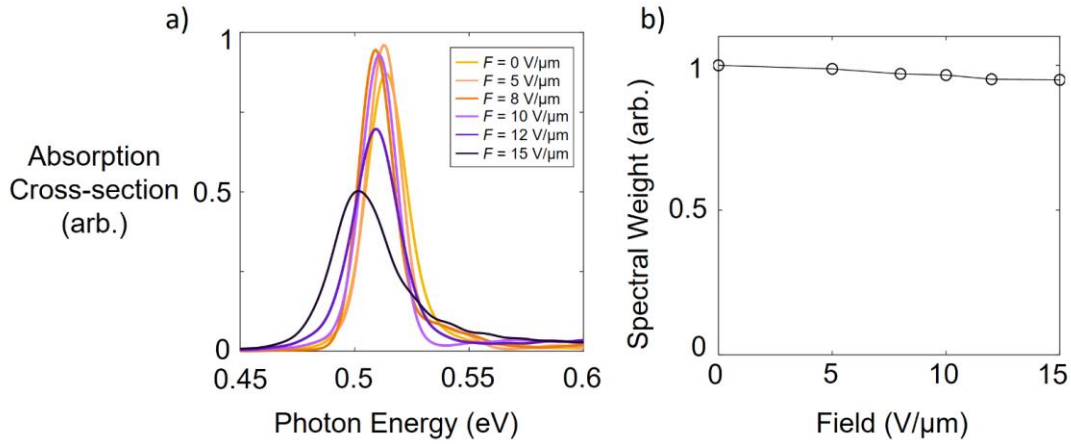


**Figure S5. a)** The calculated  $S_{22}$  absorption for a (20,16) CNT. **b)** The change in oscillator strength with field found by integrating the peaks in a).

## 5. Spectral width of exciton peaks

Figure S6a shows the FWHM of the  $S_{22}$  photocurrent peak for the eight CNTs discussed in the main text. For some CNTs in the study, the FWHM changes as a function of the axial field. In Fig. S6d we plot the calculated change in FWHM of the  $S_{22}$  absorption peak as a function of field. The calculation of the absorption spectrum is performed by applying Gaussian broadening to the solution of the Bethe-Salpeter equation for an exciton in a static electric field along the CNT axis.



From the calculation, we expect to see rapid oscillations in FWHM as a function of  $F$ . The experimental data does show non-monotonic changes in FWHM, however the step size for  $F$  in the experiment may be too large to resolve the sharp features present in the calculation. The largest experimentally observed change in FWHM at high field ( $\sim 10$  V/ $\mu\text{m}$ , shown in Fig. S6c) is on the order of 10 meV which agrees with the calculation (Fig. S6d). The sharp changes in FWHM with field seen in Fig. S6d could be due to the Franz-Keldysh oscillations<sup>2</sup> in the  $E_{11}$  continuum which overlaps in energy with the position of the  $S_{22}$  exciton.

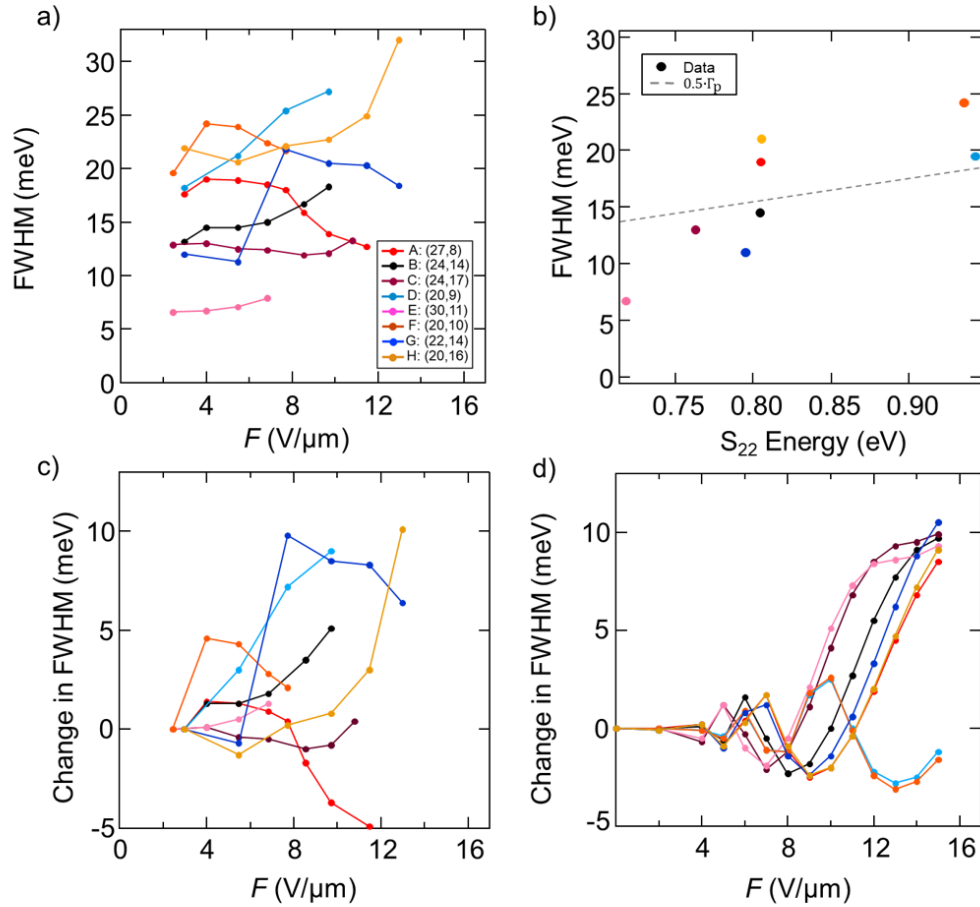


**Figure S6.** **a)** The FWHM of the  $S_{22}$  photocurrent peaks at increasing axial field for the eight different chiralities discussed in the main text. **b)** The FWHM of the  $S_{22}$  photocurrent peak with an applied axial field of 4 V/ $\mu\text{m}$ . The dashed line is the relationship in Eq. S9. **c)** The change in FWHM of the  $S_{22}$  photocurrent peaks. **d)** Calculated changes in the FWHM of the  $S_{22}$  absorption peak as a function of field for each chirality of CNT in the study. The color coding in the inset of panel (a) applies to all of the panels.

The FWHM of the  $S_{22}$  photocurrent peak is plotted as a function the peak energy in Fig. S6b. Based on previous work we expect a linear relationship between the FWHM ( $\Gamma_p$ ) and the transition energy ( $E_{\text{peak}}$ ).<sup>1,3</sup> Liu et al. found  $\Gamma_p = 0.0388 \cdot E_{\text{peak}}$ . We find that our measured FWHM values also follow a linear trend, but with overall smaller values of

$$\Gamma_p = 0.02 \cdot E_{\text{peak}} \quad (\text{S9})$$

as shown by the dashed line in Fig. S6b.

Fig. S7a shows the calculated changes in the  $S_{11}$  absorption peak with field. We do not have experimental data from  $S_{11}$  (it lies outside the spectral range of the instruments), however the calculated peak shape gives information about the field induced exciton dissociation process. Zero-field broadening of  $\Gamma_0 = 15$  meV is added to our simulation to match previous measurements by Malapanis et al.<sup>4</sup> There is a monotonic increase in FWHM with field. Fig S7a shows the  $S_{11}$  absorption peak changing with field for the largest (left) and smallest (right) diameter CNTs in the study.

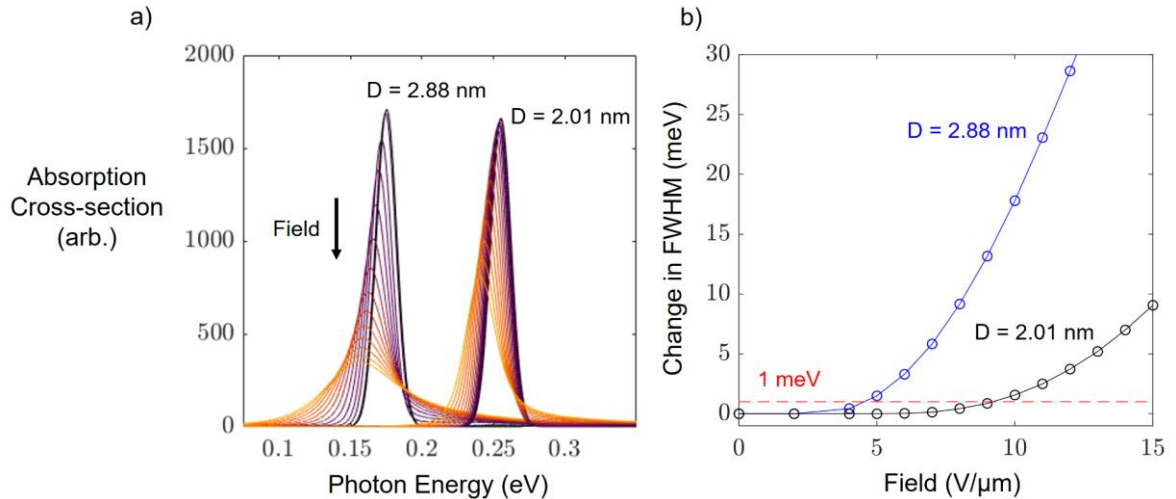


**Figure S7. a)** The calculated  $S_{11}$  absorption peak for CNT D and CNT E, the smallest and largest diameter CNTs in the study. The changing color indicated the field increasing from  $F = 0$  V/μm (violet) to  $F = 15$  V/μm (yellow). **b)** The change in FWHM for the  $S_{11}$  peaks shown in a).

Fig. S7b shows the change in the FWHM of the  $S_{11}$  peak for the same CNTs as Fig. S7a. The predicted linewidth at fields larger 5 V/μm suggests that the auto ionization broadening is at least 1 meV, which corresponds to lifetime of  $\sim 200$  fs. This is substantially lower than the estimated timescale of the non-radiative decay ( $\tau_{\text{non-rad}}$ ) discussed in the main text. This

theoretical result supports our assumption of fully ionized  $S_{11}$  excitons contributing to the photocurrent.

## 6. Self-consistent field calculations

Before starting the self-consistent cycle, we calculate the electrostatic potential in the absence of the CNT,  $V_{\text{ext}}(\mathbf{r})$ . Figure S8 shows the metallic surfaces (constant potential) that are used as boundary conditions to calculate  $V_{\text{ext}}(\mathbf{r})$ . A numerical relaxation algorithm is used to solve the 2D Laplace equation in a non-homogeneous dielectric environment

$$\frac{\partial}{\partial x} \left[ \epsilon(x, z) \frac{\partial}{\partial x} \right] V_{\text{ext}}(x, z) + \frac{\partial}{\partial z} \left[ \epsilon(x, z) \frac{\partial}{\partial z} \right] V_{\text{ext}}(x, z) = 0 \quad (\text{S10})$$

where  $\epsilon(x, z)$  is the position-dependent relative permittivity of the dielectric environment.

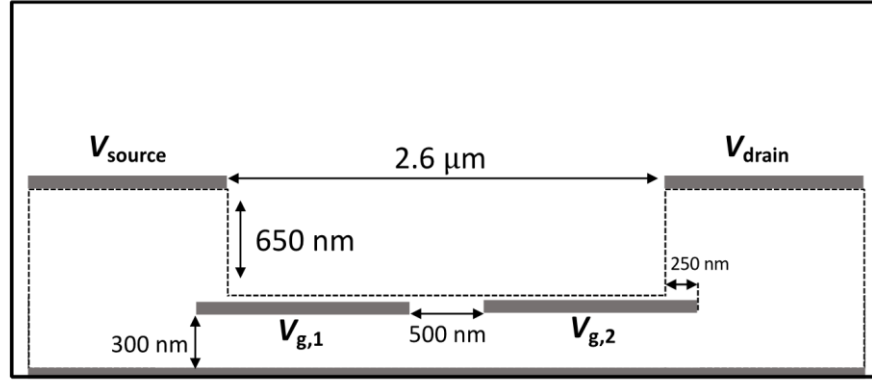


**Figure S8.** Cross sectional diagram of the dimensions used in the simulation. The metal electrode thickness is 60 nm. Dotted lines represent the  $\text{SiO}_2$  in the device. We assume translation symmetry in the third dimension.

After computing  $V_{\text{ext}}(\mathbf{r})$ , we compute the charge on the doped regions of the semiconducting CNT by means of a self-consistent cycle as follows. First, we compute the hole and electron concentrations,  $n_h(x)$  and  $n_e(x)$  respectively, as

$$n_e(x) = 2 \sqrt{\frac{m^* k_B T}{2\pi \hbar^2}} \mathcal{F}_{-\frac{1}{2}} \left( \frac{\mu_e - E_c(x)}{k_B T} \right) \quad \text{S11}$$

$$n_h(x) = 2 \sqrt{\frac{m^* k_B T}{2\pi \hbar^2}} \mathcal{F}_{-\frac{1}{2}} \left( \frac{\mu_h - E_v(x)}{k_B T} \right) \quad \text{S12}$$

where  $m^*$  is the effective mass of electrons and holes,  $T$  is the temperature,  $\mu_e$  is the quasi-Fermi level for electrons,  $\mu_h$  is the quasi-Fermi level for holes, and  $\mathcal{F}_{1/2}$  is the complete Fermi-Dirac integral of order -1/2. For the semiconducting CNT, we assume the following relationship between  $m^*$  and the CNT band gap:

$$m^* = \frac{E_g}{v_F^2} \approx m_e \frac{E_g}{[7 \text{ eV}]} \quad (\text{S13})$$

Figure 2b in the main text shows the net charge (linear charge density) which is given by

$$\lambda(x) = e(n_h(x) - n_e(x)). \quad (\text{S14})$$

At each point on the CNT, we assume that charge is spread uniformly around the circumference of the CNT. This charge density,  $\lambda(x)$ , generates an electrostatic potential  $V_{\text{int}}(\mathbf{r})$  which modifies the total electrostatic potential in the self-consistent cycle. The latter potential along the length of the CNT is given by

$$V_{\text{tot}}(x) = V_{\text{ext}}(x) + V_{\text{int}}(x). \quad (\text{S15})$$

From  $V_{\text{tot}}(x)$ , we find the energy of the valence band edge,  $E_v(x)$ , and the energy of the conduction band edge,  $E_c(x)$ . In order to model the reverse-bias condition, the quasi Fermi level for holes is pinned mid gap at the left electrode and the quasi Fermi level for electrons is pinned mid gap at the right electrode. Thus,

$$E_v(x) = eV_{\text{tot}}(x) - \frac{E_g}{2} \quad (\text{S16})$$

$$E_c(x) = eV_{\text{tot}}(x) + \frac{E_g}{2}. \quad (\text{S17})$$

Figure S9 shows the self-consistent band diagram at room temperature for  $E_v(x)$  and  $E_c(x)$  that go together with Fig. 2c in the main text. The split-gate voltages induce hole accumulation on the left side and electron accumulation on the right side. An insulating intrinsic region is formed in the central part, where the two bands show a linear dependence on the position.

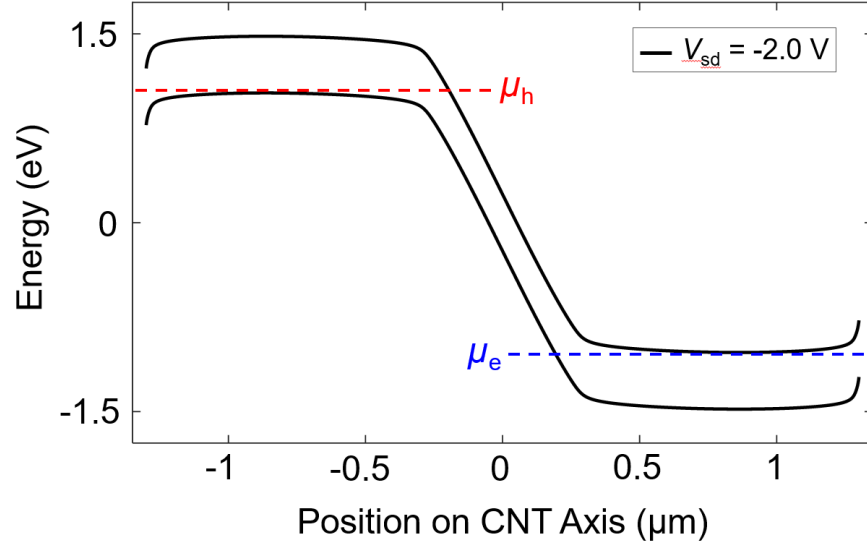


**Figure S9.** The energy bands along the length of the nanotube from SCF calculations. The chemical potential for holes,  $\mu_h$ , is in equilibrium with the left electrode. The chemical potential for electrons,  $\mu_e$ , is in equilibrium with the right electrode. In the middle of the CNT an insulating region is formed.

## 7. Imaging the intrinsic region length

The length of the intrinsic region,  $L_i$ , can be measured in scanning photocurrent microscopy (SPCM) images whenever  $L_i$  is larger than the laser spot.<sup>5</sup> Here we describe our process to determine  $L_i$  from SPCM images such as Fig. 2f in the main text. We used these measured values of  $L_i$  to verify the electrostatics model at particular values of  $V_{sd}$  and  $V_{g1} = -V_{g2}$ .

Figure S\_ illustrates the process of extracting  $L_i$  from a pair of SPCM images. Both images were taken in an ambient environment at room temperature. The first image (Fig. S10a) reveals the axis of the CNT. The image is acquired by setting  $V_{sd} = 0$  and  $V_{g1} = -V_{g2} = 0$ . Positive current is generated at one end of the CNT by the electric field associated with the Schottky barrier contact. Negative current is generated at the other end of the CNT by the other Schottky barrier contact (electric field pointing in the reverse direction). The dashed lines in Fig. S10a correspond to the edge of the metal electrodes. The electrode edges are determined from the reflection image (Fig. S10c) which was acquired simultaneously. The second SPCM image (Fig. S10b) shows the photocurrent generated by the photodiode. A pn junction was established in the center of the CNT by setting  $V_{g1} = -V_{g2} = 6$  V. The intrinsic region is elongated by applying a reverse bias  $V_{sd} = -3$  V. Figure S10d shows a cross-section of the photocurrent image, taken along the CNT axis.

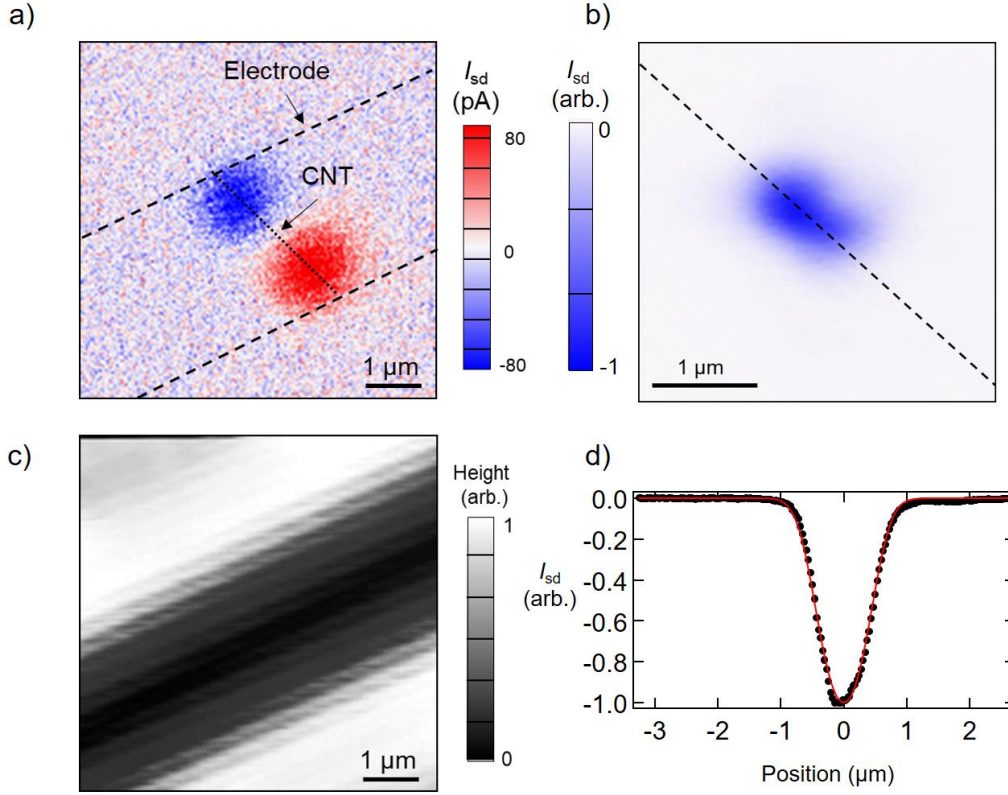


**Figure S10** **a)** Scanning photocurrent image of the Schottky barriers at each contact with  $V_{sd} = 0$  and  $V_{g1} = V_{g2} = 0$ . The axis of the CNT is indicated with a dotted line. **b)** Scanning photocurrent image of an elongated photocurrent spot when  $V_{sd} = -3$  V and  $V_{g1} = -V_{g2} = 6$  V. **c)** An image of the reflected light from the scanning photocurrent image. The images shows the edges of the electrodes (white) the gate electrodes (grey) and the gap between the gate electrodes (black). **d)** A cross section of the photocurrent image shown in b) along the CNT axis. The fit from Eq. S20 is shown in red for  $L = 0.9$   $\mu\text{m}$  and  $a = 0.347$   $\mu\text{m}$ .

The photocurrent cross-section (shown in Figure 10d) is a convolution of the point spread function (PSF) of the laser spot and the position-dependent quantum yield,  $\eta(x)$ , of the CNT. Along the axis of the CNT (the  $x$  direction), the PSF of the laser spot is treated as a Gaussian given by

$$f(x) = \exp\left(-\frac{x^2}{a^2}\right). \quad (\text{S18})$$

We estimate  $\eta(x)$  as a top-hat function

$$\eta(x) = \begin{cases} 0 & \text{when } x < -L_i/2 \\ \eta_0 & \text{when } -L_i/2 < x < L_i/2. \\ 0 & \text{when } x > L_i/2 \end{cases} \quad (\text{S19})$$

The expected photocurrent profile along the axis of the CNT,  $I_{sd}(x)$ , is then a convolution of  $f(x)$  and  $\eta(x)$

$$I_{sd}(x) \propto \operatorname{erf}\left(\frac{x - \frac{L_i}{2}}{a}\right) - \operatorname{erf}\left(\frac{x + \frac{L_i}{2}}{a}\right). \quad (\text{S20})$$

To determine intrinsic region length from Fig S10d, we fit Eq. S20, using  $L_i$  and peak current as fitting parameters. We note that Eq. S20 becomes indistinguishable from a Gaussian when  $L_i < a$ , therefore, fitted values of  $L_i$  are only reliable for  $L_i \gtrsim 2a$ .

Figure S11a and c show the cross-sections of photocurrent images of pn junctions corresponding to various  $V_{g1} = -V_{g2}$  and  $V_{sd}$ . Figure S11a shows the decrease in  $L_i$  as  $V_{g1} = V_{g2}$  increases. Figure S11c shows the increase in  $L_i$  as  $|V_{sd}|$  increases. In both Figures, we note that the width of the peak stops changing when  $L_i \lesssim 2a$ , due to the spatial resolution of our microscope. Figure S11d compares the fitted value of  $L_i$  (from S11a) with the model described in the main text (Eq. 2). We see excellent agreement between experiment and modeling when  $L_i > 600$  nm, giving us confidence in the electrostatics modeling.

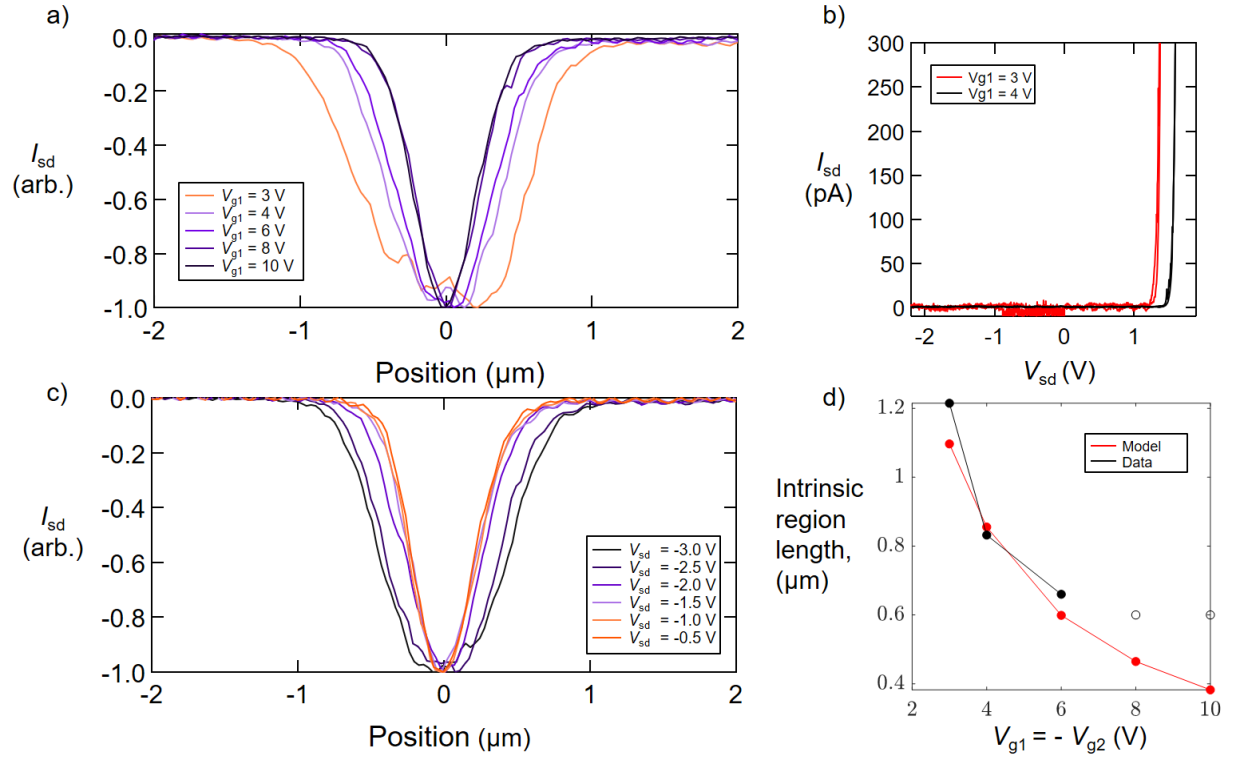


**Figure S11** **a)** Cross sections of photocurrent images along the CNT axis for various  $V_{g1} = -V_{g2}$ .  $V_{sd} = -2$  V for all 5 curves. **b)** Diode characteristics at the highest ratios of  $V_{sd}/V_{g1}$  used in (a). There is no reverse-bias break down. **c)** Cross sections of photocurrent images along the CNT axis at various  $V_{sd}$ .  $V_{g1} = -V_{g2} = 6$  V for all 6 curves. **d)** Comparison of the model in Eq. 2 of the main text (red) with experimental measurement of  $L_i$  extracted from the cross sections shown in (a) (black). The fitting procedure to find  $L_i$  becomes unreliable when  $V_{g1} > 6$  V (open circles), because  $L_i$  is below the spatial resolution of the microscope. The nanotube chirality is (17,12).

## 8. Intrinsic region length determined from electrostatic modeling

Figure S12a illustrates our method for extracting  $L_i$  from our SCF electrostatics simulations. The linear charge density in the CNT,  $\lambda(x)$ , is plotted for various values of  $V_{sd}$  when  $V_{g1} = -V_{g2} = 4$  V. We consider  $\lambda(x)$  near the center of the CNT in a limited range  $-10e \mu\text{m}^{-1} < \lambda(x) < 10e \mu\text{m}^{-1}$ . When  $10e \mu\text{m}^{-1} > \lambda > 1e \mu\text{m}^{-1}$ ,  $\lambda$  changes linearly with respect to position. We extrapolate this linear relationship to the x-axis and thus define the edge of the intrinsic region. Repeating this process on the right edge of this intrinsic region then determines  $L_i$ .



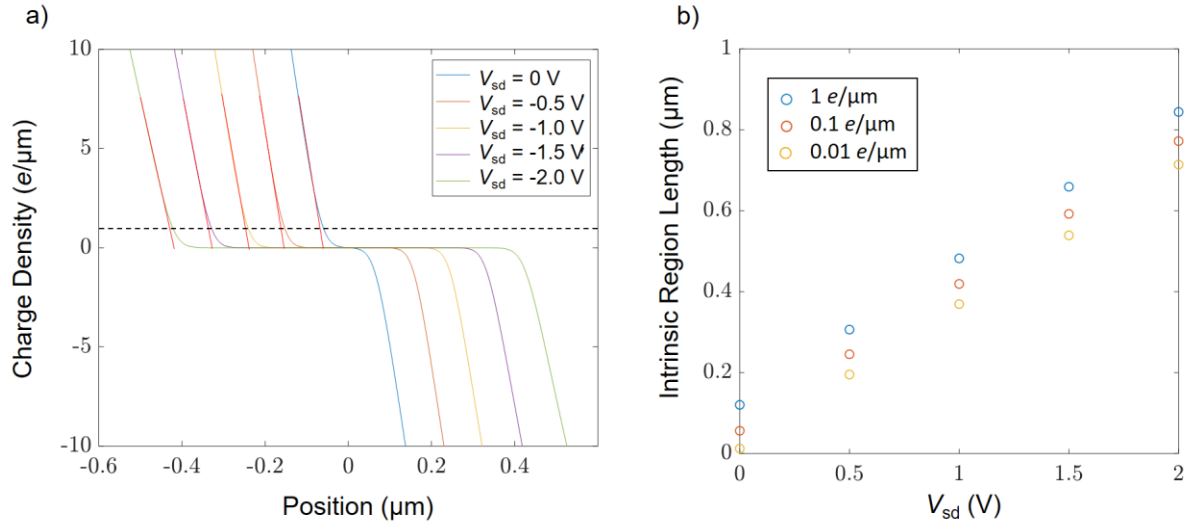


**Figure S12 a)** The charge density along the length of the CNT. Linear fits (red) are extrapolated to the x-axis to find the edge of the intrinsic region with  $V_{g1} = 4$  V. The dashed line shows the value is comparable to using a cutoff charge density of  $1 e \mu\text{m}^{-1}$ . **b)** The calculated intrinsic region length using different cutoff charge densities.

Our extrapolation method is equivalent to setting a threshold  $|\lambda| < 1 e \mu\text{m}^{-1}$  to define the intrinsic region. We have tried with other threshold levels. Figure S12b shows the measured intrinsic region lengths for a threshold of  $1 e \mu\text{m}^{-1}$ ,  $0.1 e \mu\text{m}^{-1}$ , and  $0.01 e \mu\text{m}^{-1}$ . Reducing the threshold level reduces the calculated length of the intrinsic region. For our analysis of photocurrent quantum yield (PCQY), we prefer a conservative estimate of  $L_i$  that will not inflate our values of PCQY. Therefore, we used the linear extrapolation method (Fig. S12a) which results in the largest estimate of  $L_i$ .

## 9. Cross-check of calculated charge density

To verify the validity of the results from the SCF calculation we consider the capacitance determined by the calculation. Figure S13a displays the SCF calculation results for the charge density of the nanotube in a pn junction configuration at various gate voltage. Figure S13b shows the maximum charge density on the p doped side of the nanotube. The maximum capacitance per length can be found from the slope of the line which gives  $C_L = 2.7 \text{ aF}/\mu\text{m}$  for the nanotube.

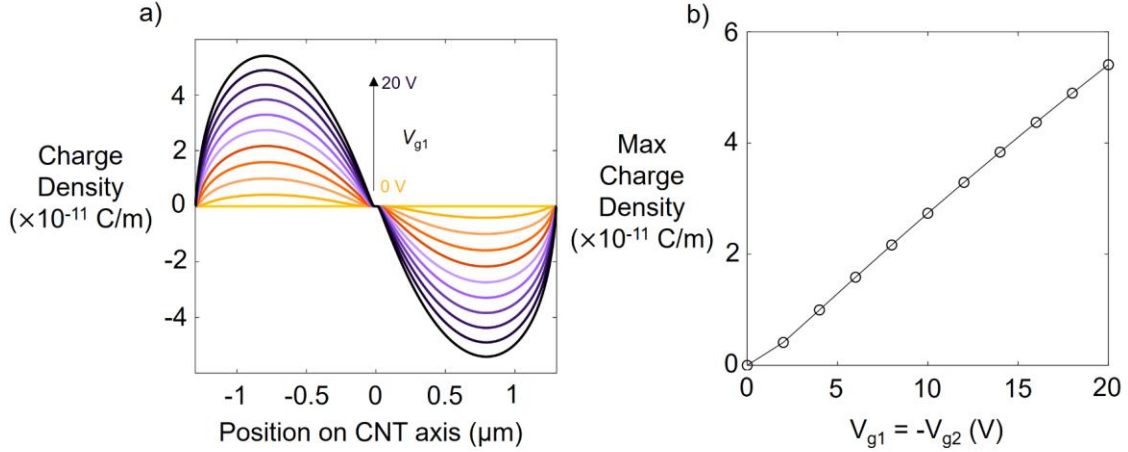


**Figure S13. a)** The charge density along the length of the nanotube as a function of gate voltage with  $V_{sd} = 0$  V. **b)** The maximum charge density in p doped portion of the nanotube extracted from the SCF simulations shown in a).

An upper bound for the capacitance of the nanotube can be calculated using the simple case of an infinitely long wire over a conducting plane. The capacitance per length of our actual device will be less than that of an infinite wire because each side of the nanotube has some coupling to gate on the other side. The potential,  $V$ , of a wire with charge density  $\lambda$  can be found by first using method of images to treat the conducting plane as a mirror charge and then using Gauss's law to find the electric field of the two charged wires. Integrating the field gives the potential

$$V = \frac{\lambda \cdot L \cdot \ln \frac{4h}{D}}{2\pi\epsilon_0\epsilon_r} \quad (\text{S21})$$

where  $h$  is the tube height, and  $D$  is the diameter of the wire. The capacitance per length is then

$$C_L = \frac{2\pi\epsilon_0\epsilon_r}{\ln \frac{4h}{D}}. \quad (\text{S22})$$

For  $h = 650$  nm and  $D = 2 - 3$  nm the capacitance is  $C_L = 7.76 - 8.22$  aF/ $\mu\text{m}$ . The capacitance in the SCF calculation is the same order of magnitude but lower as expected.

A more realistic upper bound can be found through Coulomb blockade spectroscopy of devices with a single back gate. For a single gate device with a 2 micron long CNT suspended 750 nm above the gates, we have measured the capacitance to be  $C_L = 3.5$  aF/ $\mu\text{m}$ .<sup>5</sup> In this work we are considering the capacitance of half of a split-gate device, therefore, we explicit slightly lower capacitance than a full single gate device.

## 10. Cross check for photo-conductance

The magnitude of the signal when taking a photocurrent spectrum was typically  $\sim 10$  pA, near the limit of our instruments. A moderate reverse bias of  $V_{sd} = -0.5$  V was applied to increase the signal. While this introduces the possibility of photo-conductance, we don't find any evidence of a photo-conductance mechanism.

Fig. S14 shows illuminated  $I/V$  curves for two CNTs at the  $S_{22}$  resonance. As discussed in the main text, we expect a linear increase in photocurrent with increasing reverse bias as the intrinsic region of the CNT elongates. To first approximation, we expect photocurrent quantum yield (PCQY) to be independent of  $V_{sd}$ . In Fig. S14 we show lines of best fit (red dashed lines) based on Eqs. 1 and 2 of the main text with  $\eta_{22} = \text{constant}$ . Our procedure for extracting PCQY from the experimental data would give the same result for any  $V_{sd}$  between 0 and -0.5 V.

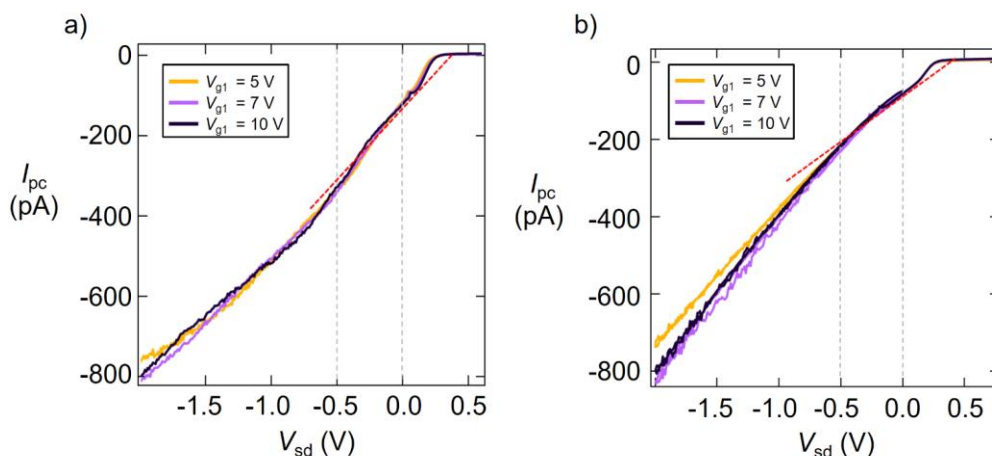


**Figure S14.** **a)** Illuminated  $I/V$  curve of a (22,11) CNT excited at the resonance  $S_{22} = 0.86$  eV. **b)** Illuminated  $I/V$  curve of a (23,12) CNT excited at the resonance  $S_{22} = 0.795$  eV.

## 11. Nanotube growth

A square of iron catalyst is deposited on top of the source and drain electrodes  $2\ \mu\text{m}$  from the edge of the trench by patterning a photoresist mask and evaporating 2 nm of Ti, 30 nm of  $\text{SiO}_2$ , and then 2 nm of Fe. The chip is placed inside of a one-inch diameter quartz tube within a tube furnace. Prior to heating the furnace, the chamber is purged for 3 minutes with the growth gasses. The chip is left in the cool region of quartz tube (outside the furnace) while the furnace heats to  $800\ ^\circ\text{C}$ . Once the furnace reaches  $800\ ^\circ\text{C}$ , the chip is shuttled into the hot zone of the tube furnace

and annealed in  $H_2$  gas for 1 minute (0.45 SLM) to chemically reduce the Fe catalyst. While the chip is in the hot zone, the gases are switched to a 2:1 mixture of ethanol and methanol vapor carried by Ar and  $H_2$ .<sup>6</sup> To create this growth gas, Ar is bubbled through reservoirs of liquid ethanol and methanol (the ethanol and methanol are kept at room temperature). Ar is bubbled through ethanol at a rate of 0.15 SLM and Ar is bubbled through methanol at a rate of 0.3 SLM. The Ar + ethanol vapor, Ar + methanol vapor are combined with  $H_2$  flowing at 0.45 SLM. The total flow rate of growth gases is 0.9 SLM. After 5 minutes, the gas flow is switched to 1 SLM Ar. The chip is promptly shuttled back into the cool region of the tube.

## **12. Extended data for devices A-J**

(see next page)

### Extended Data for Device A

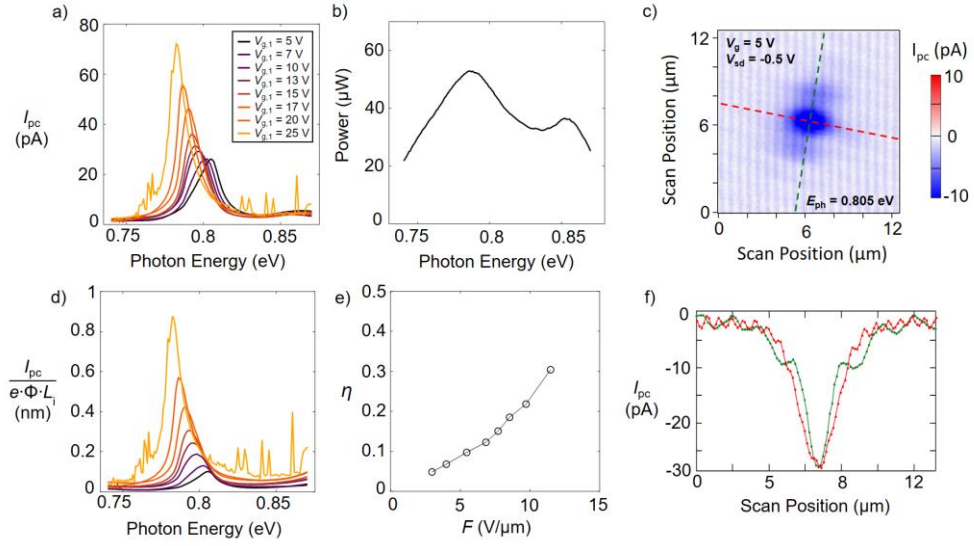


**Fig. S15 Device A Summary** a) Raw photocurrent spectrum of a (27,8) carbon nanotube. b) Laser power at the height of nanotube. c) Photocurrent image of the nanotube. The power is  $P = 2.02 \mu\text{W}$  with  $\beta_{\text{foc}} = 1.07$ . d) The photocurrent spectrum corrected for photon flux and intrinsic region length. e) The photocurrent quantum yield as a function of the axial field at the center of the CNT. f) Cross sections along the photocurrent spot used to calculate an area  $A = 6.7 \mu\text{m}^2$ .

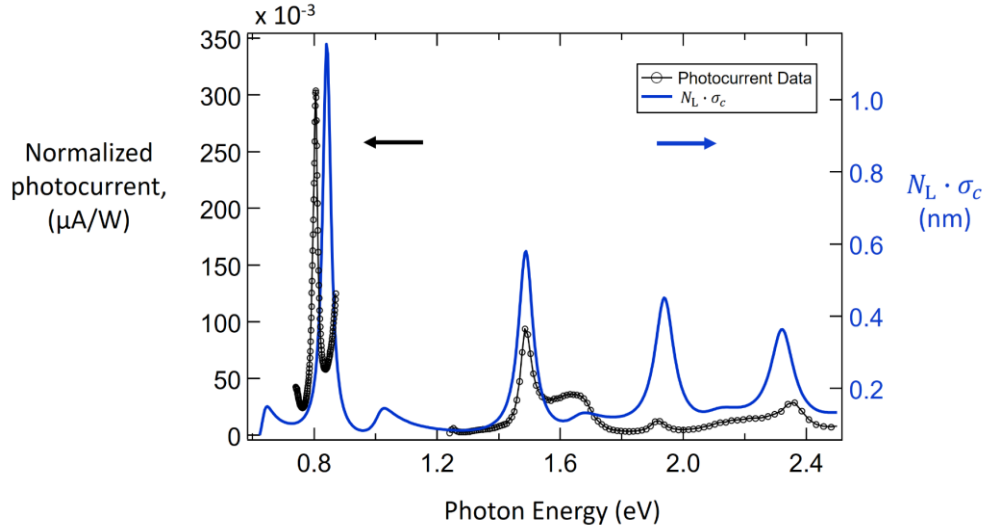


**Fig. S16** Photocurrent spectrum normalized by the laser power at the height of the nanotube 34 nm below the electrode (black). The product of absorption cross section per carbon atom and the number of atoms per length of a (27,8) CNT (blue).

$w_{y,0} (\mu\text{m})$	$a_{x,1}$	$a_{x,-1}$	$w_{x,0} (\mu\text{m})$	$w_{x,1} (\mu\text{m})$	$w_{x,-1} (\mu\text{m})$
1.49	0.29	0.32	0.88	0.89	0.93

**Table S1** The fitting parameters for scanning photocurrent image cross sections for device A. The extra lobes in the photocurrent image are fit using three Gaussians. The total area under them is  $A_{\text{foc}} = \pi w_{y,0}(w_{x,0} + a_{x,1}w_{x,1} + a_{x,-1}w_{x,-1})$ .

## Extended Data for Device B

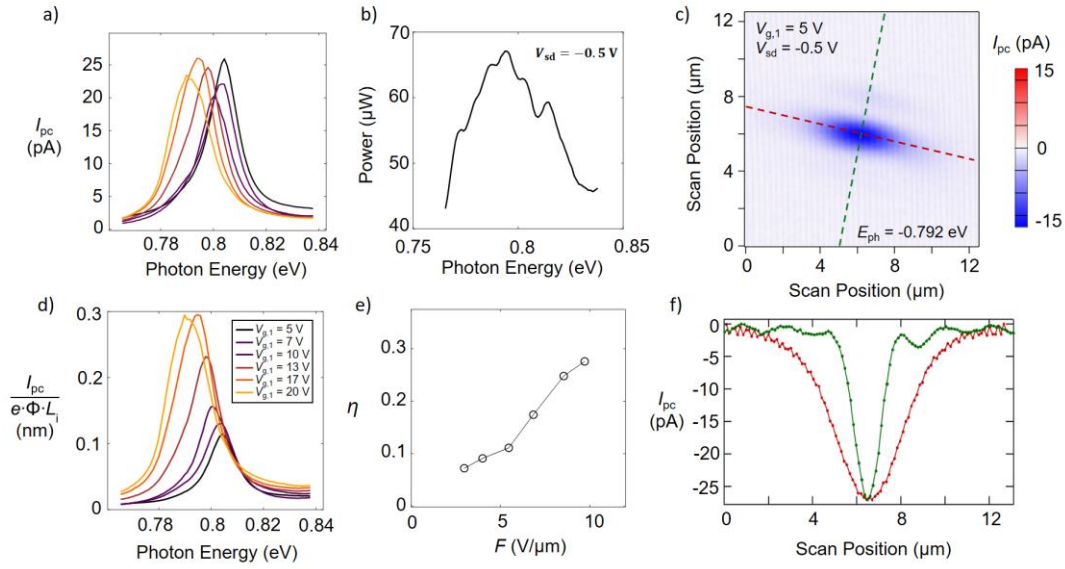


**Fig. S17 Device B Summary** a) The photocurrent spectrum of a (24,14) CNT. b) Laser power at the height of nanotube at 34 nm below the electrode surface. c) Photocurrent image of the nanotube. The power is  $P = 8.36 \mu\text{W}$  with  $\beta_{\text{foc}} = 1.14$ . d) The photocurrent spectrum corrected for photon flux and intrinsic region length. e) The photocurrent quantum yield as a function of the axial field at the center of the CNT. f) Cross sections along the photocurrent spot used to calculate an area  $A = 5.4 \mu\text{m}^2$ .

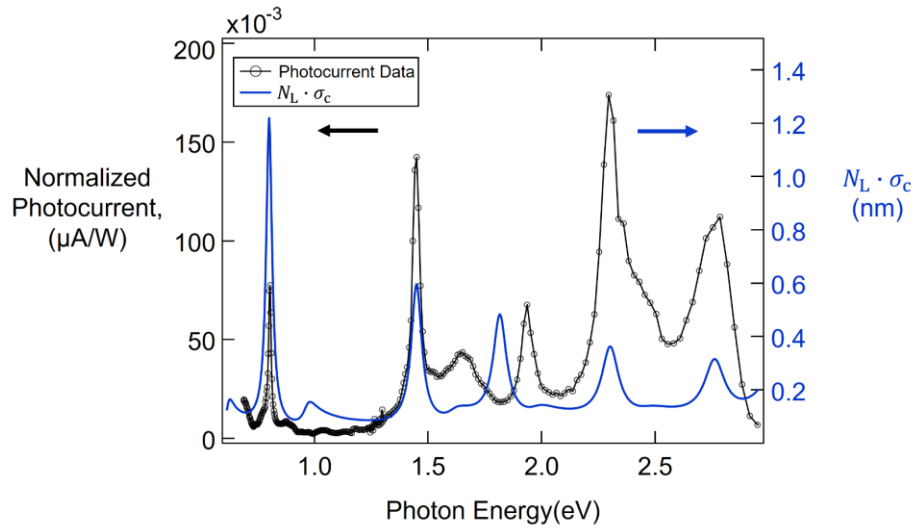


**Fig. S18** Photocurrent spectrum normalized by the laser power at the height of the nanotube 34 nm below the electrode (black). The product of absorption cross section per carbon atom and the number of atoms per length of a (24,14) CNT (blue).

### Extended Data for Device C

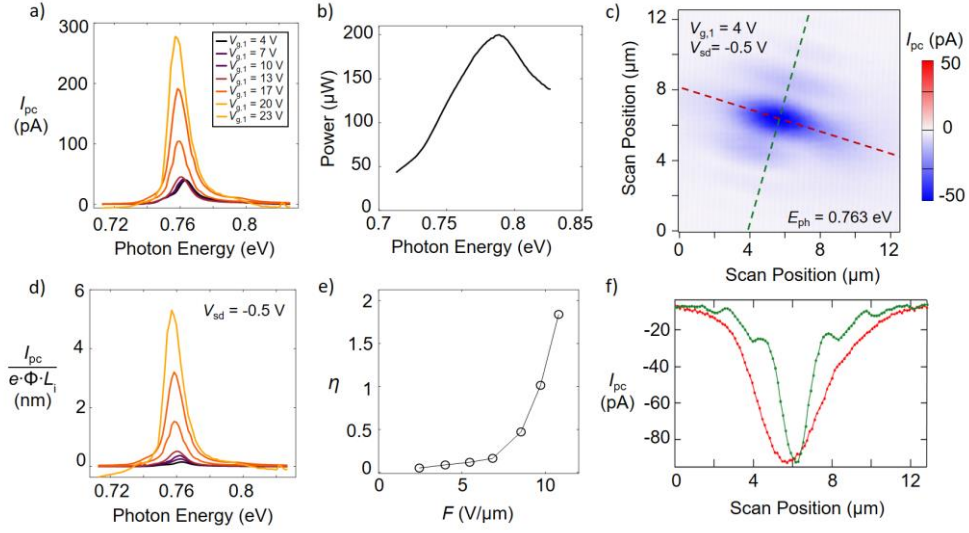


**Fig. S19 Device C Summary** Raw photocurrent spectrum of a (24,17) carbon nanotube. b) Laser power at the height of nanotube at 34 nm below the electrode surface. c) Photocurrent image of the nanotube. The power is  $P = 23.1 \mu\text{W}$  with  $\beta_{\text{foc}} = 1.31$ . d) The photocurrent spectrum corrected for photon flux and intrinsic region length. e) The photocurrent quantum yield as a function of the axial field at the center of the CNT. f) Cross sections along the photocurrent spot used to calculate an area  $A = 9.1 \mu\text{m}^2$ .

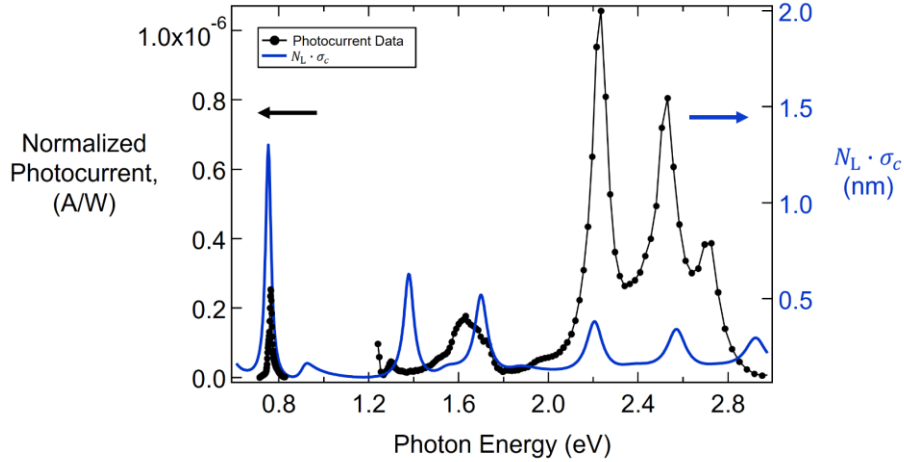


**Fig. S20** Photocurrent spectrum normalized by the laser power at the height of the nanotube 34 nm below the electrode (black). The product of absorption cross section per carbon atom and the number of atoms per length of a (24,17) CNT (blue).

$w_{y,0} (\mu\text{m})$	$a_{x,1}$	$a_{x,-1}$	$w_{x,0} (\mu\text{m})$	$w_{x,1} (\mu\text{m})$	$w_{x,-1} (\mu\text{m})$
2.38	0.20	0.17	0.99	0.84	0.94

**Table S2** The fitting parameters for scanning photocurrent image cross sections for Device C. The extra lobes in the photocurrent image can be well fit using three Gaussians. The total area under them is  $A_{\text{foc}} = \pi w_{y,0} (w_{x,0} + a_{x,1} w_{x,1} + a_{x,-1} w_{x,-1})$ .

### Extended Data for Device D

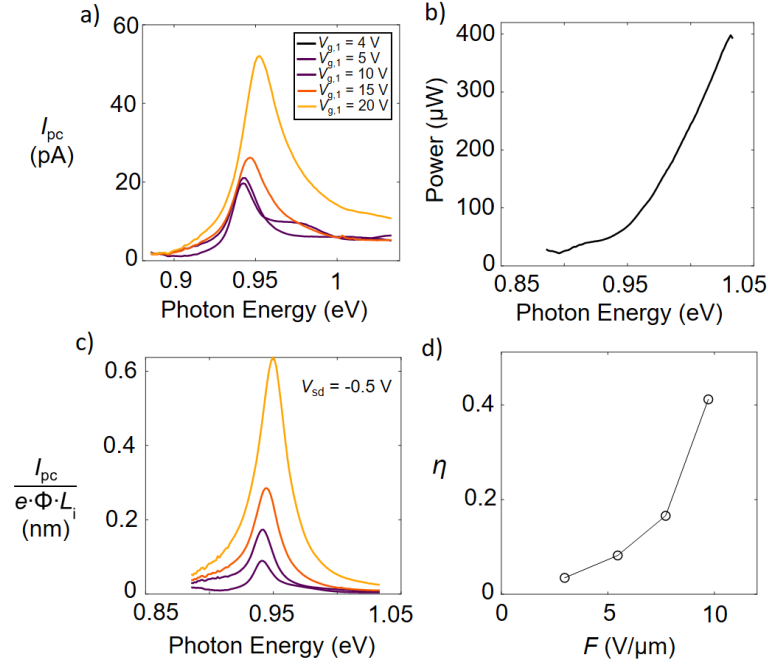


**Fig. S21 Device D Summary** Raw photocurrent spectrum of a (20,9) carbon nanotube. b) Laser power at the height of nanotube at 34 nm below the electrode surface. c) The photocurrent spectrum corrected for photon flux and intrinsic region length. d) The photocurrent quantum yield as a function of the axial field at the center of the CNT.

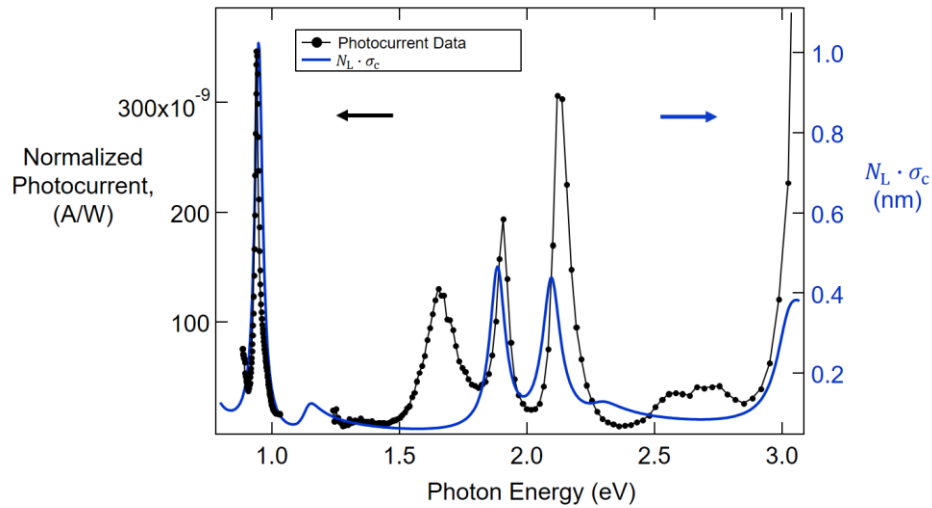


**Fig. S22** Photocurrent spectrum normalized by the laser power at the height of the nanotube 34 nm below the electrode (black). The product of absorption cross section per carbon atom and the number of atoms per length of a (20,9) CNT (blue).



### Extended Data for Device E

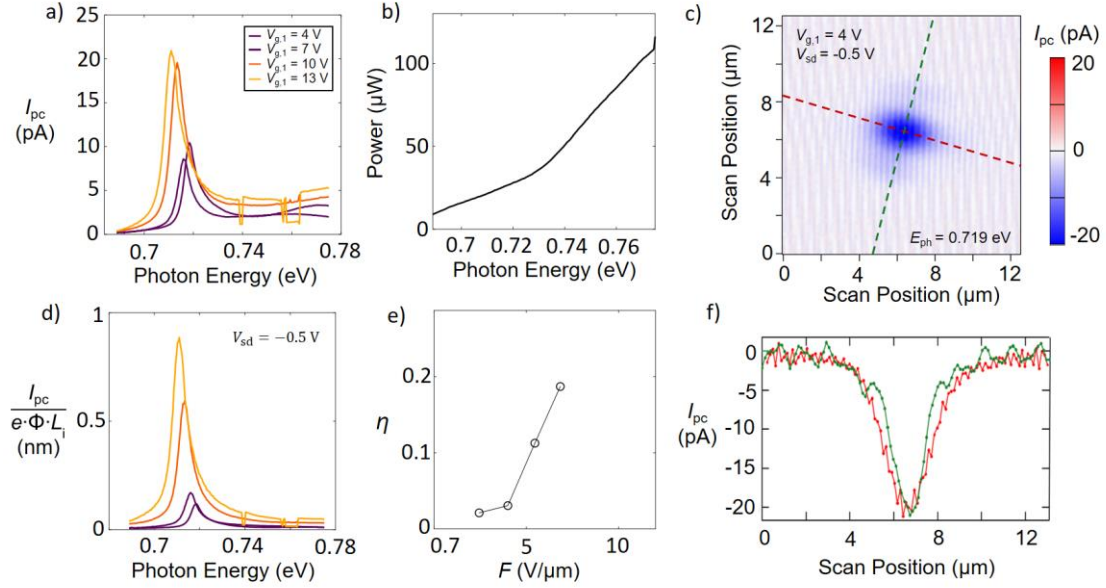


**Fig. S23 Device E Summary** Raw photocurrent spectrum of a (30,11) carbon nanotube. b) Laser power at the height of nanotube at 34 nm below the electrode surface. c) Photocurrent image of the nanotube. The power is  $P = 1.63 \mu\text{W}$  with  $\beta_{\text{foc}} = 1.52$ . d) The photocurrent spectrum corrected for photon flux and intrinsic region length. e) The photocurrent quantum yield as a function of the axial field at the center of the CNT. f) Cross sections along the photocurrent spot used to calculate an area  $A = 5.4 \mu\text{m}^2$ .

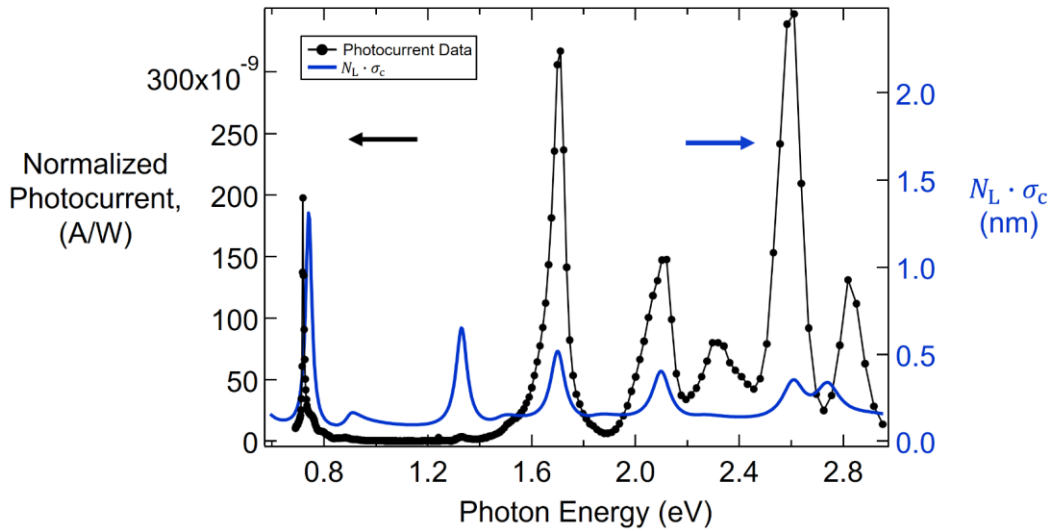


**Fig. S24** Photocurrent spectrum normalized by the laser power at the height of the nanotube at 34 nm below the electrode (black). The product of absorption cross section per carbon atom and the number of atoms per length of a (30,11) CNT (blue).

### Extended Data for Device F

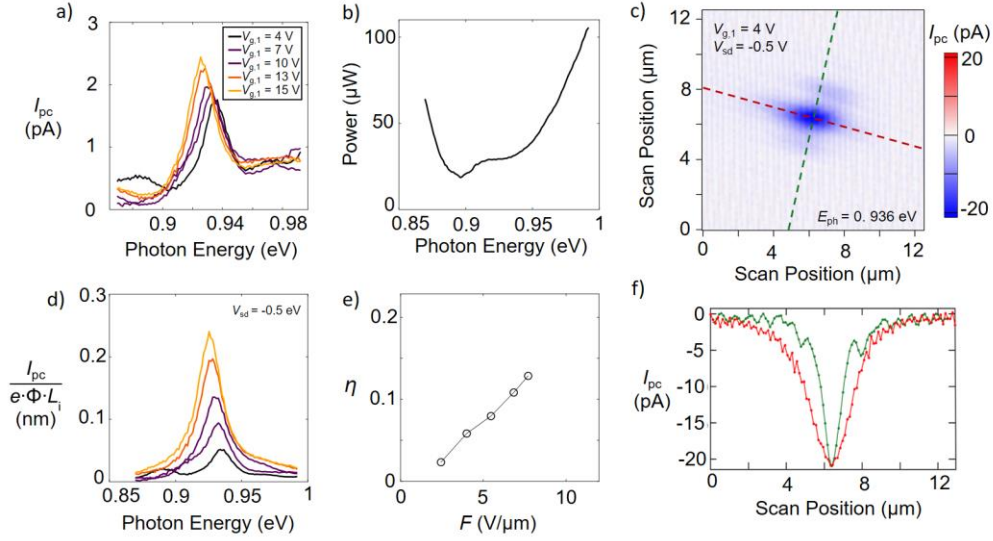


**Fig. S25 Device F Summary** Raw photocurrent spectrum of a (20,10) carbon nanotube. b) Laser power at the height of nanotube at 34 nm below the electrode surface. c) Photocurrent image of the nanotube. The power is  $P = 5.6 \mu\text{W}$  with  $\beta_{\text{foc}} = 0.49$ . d) The photocurrent spectrum corrected for photon flux and intrinsic region length. e) The photocurrent quantum yield as a function of the axial field at the center of the CNT. f) Cross sections along the photocurrent spot used to calculate an area  $A = 5.5 \mu\text{m}^2$ .

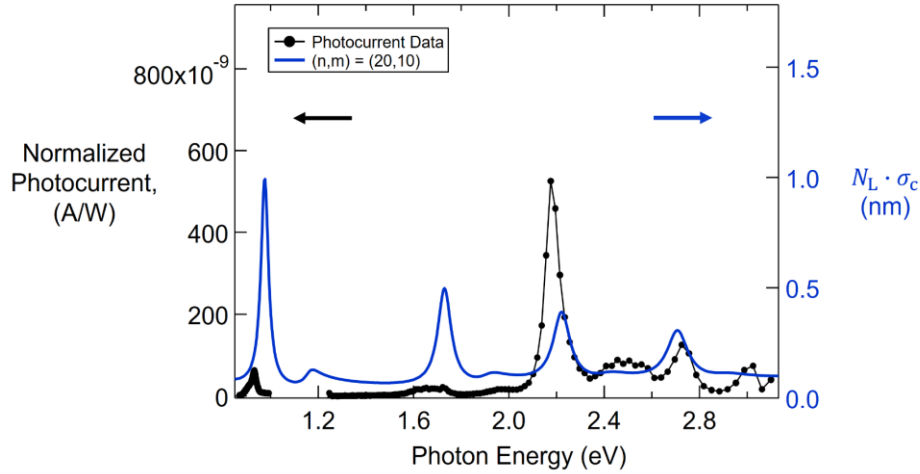


**Fig. S26** Photocurrent spectrum normalized by the laser power at the height of the nanotube 34 nm below the electrode (black). The product of absorption cross section per carbon atom and the number of atoms per length of a (20,10) CNT (blue).

$w_{y,0} (\mu\text{m})$	$a_{x,1}$	$a_{x,-1}$	$w_{x,0} (\mu\text{m})$	$w_{x,1} (\mu\text{m})$	$w_{x,-1} (\mu\text{m})$
1.66	0.25	0.16	0.79	0.69	0.68

**Table S3** The fitting parameters for scanning photocurrent image cross sections for Device F. The extra lobes in the photocurrent image can be well fit using three Gaussians. The total area under them is  $A_{\text{foc}} = \pi w_{y,0} (a_{x,0} w_{x,0} + a_{x,1} w_{x,1} + a_{x,-1} w_{x,-1})$ .

### Extended Data for Device G

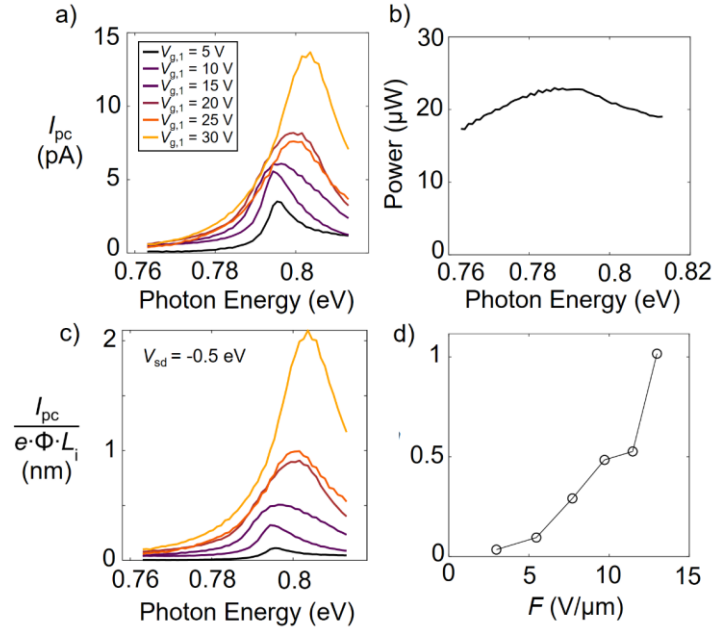


**Fig. S27 Device G Summary** a) Raw photocurrent spectrum of a (22,14) carbon nanotube. b) Laser power at the height of nanotube at 34 nm below the electrode surface. c) The photocurrent spectrum corrected for photon flux and intrinsic region length. d) The photocurrent quantum yield as a function of the axial field at the center of the CNT.

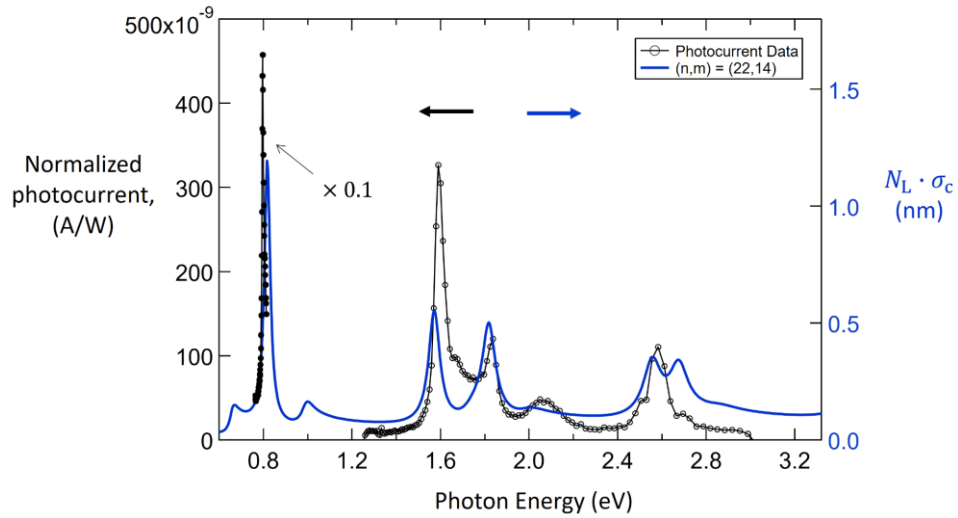


**Fig. S28** Photocurrent spectrum normalized by the laser power at the height of the nanotube 34 nm below the electrode (black). The product of absorption cross section per carbon atom and the number of atoms per length of a (22,14) CNT (blue).

### Extended Data for Device H

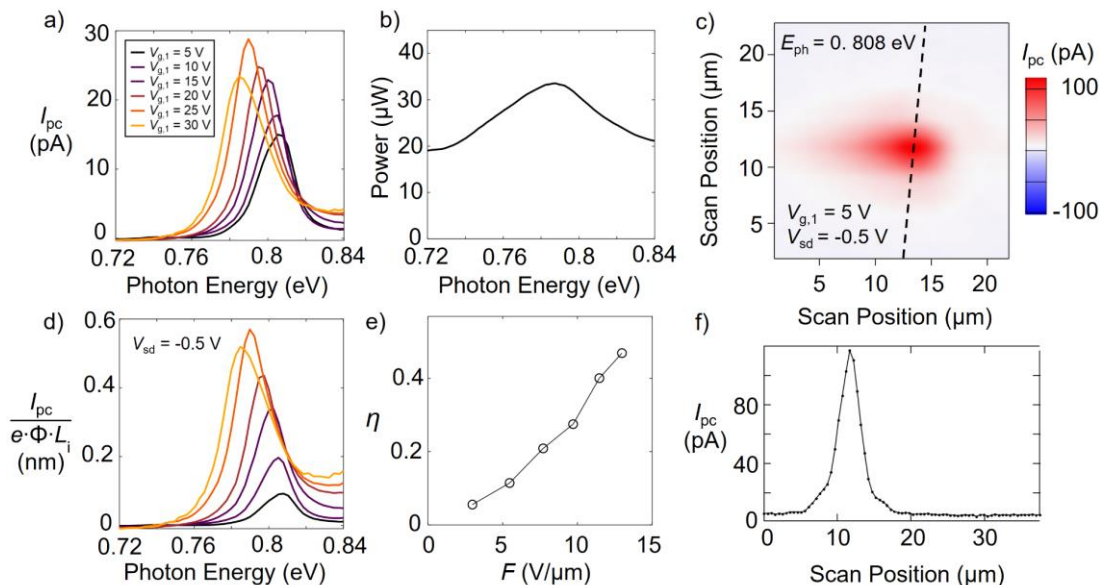


**Fig. S29 Device H Summary** The photocurrent spectrum of a (20,16) carbon nanotube. b) Laser power at the height of nanotube at 34 nm below the electrode surface. c) Photocurrent image of the nanotube. The power is  $P = 44.3 \mu\text{W}$  with  $\beta_{\text{foc}} = 1.05$ . d) The photocurrent spectrum corrected for photon flux and intrinsic region length. e) The photocurrent quantum yield as a function of the axial field at the center of the CNT. f) Cross sections along the photocurrent spot used to calculate an area  $A = 15.2 \mu\text{m}^2$ .

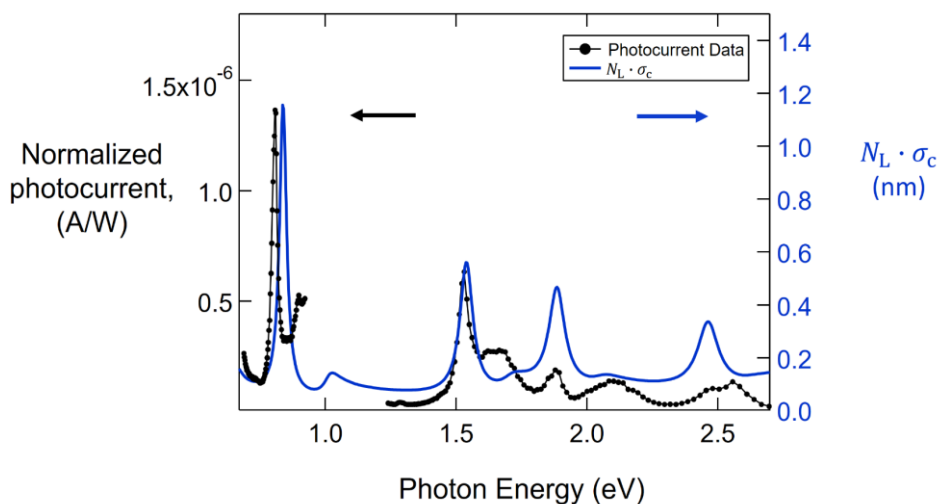


**Fig. S30** Photocurrent spectrum normalized by the laser power at the height of the nanotube 34 nm below the electrode (black). The product of absorption cross section per carbon atom and the number of atoms per length in the nanotube (blue).

### Extended Data for Device J

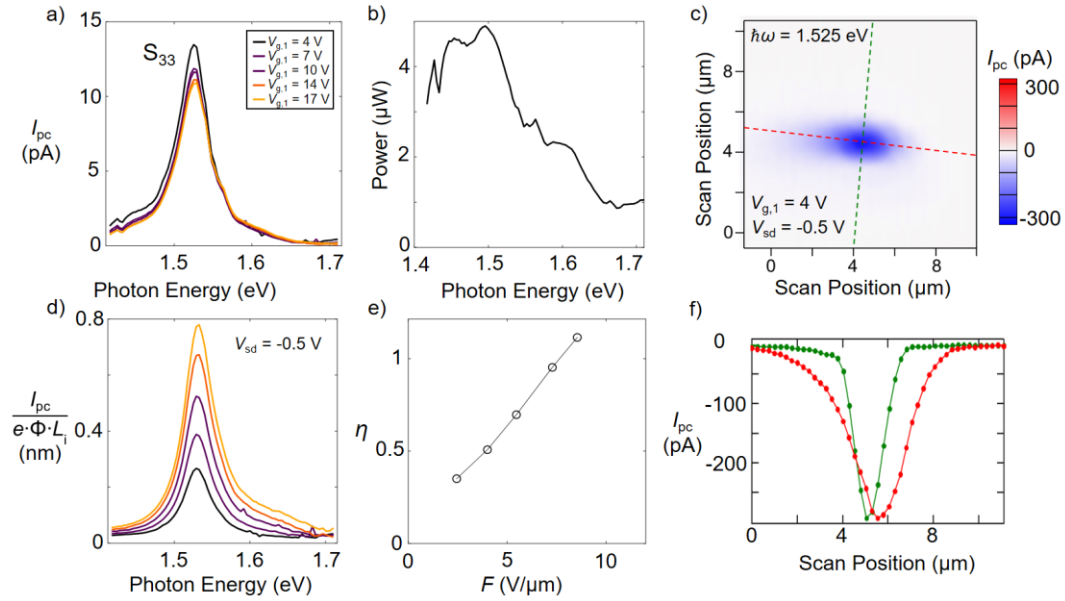


**Fig. S31 Device J Summary** Raw photocurrent spectrum of a (19,18) carbon nanotube. b) Laser power at the height of nanotube at 34 nm below the electrode surface with  $\beta_{\text{foc}}/\beta_{\text{def}} = 1.62$ . c) Photocurrent image of the nanotube. The power is  $P = 46.8 \mu\text{W}$  with  $\beta_{\text{foc}} = 1.41$ . d) The photocurrent spectrum corrected for photon flux and intrinsic region length. e) The photocurrent quantum yield as a function of the axial field at the center of the CNT. f) Cross sections along the photocurrent spot were used to calculate an area  $A = 4.92 \mu\text{m}^2$ .

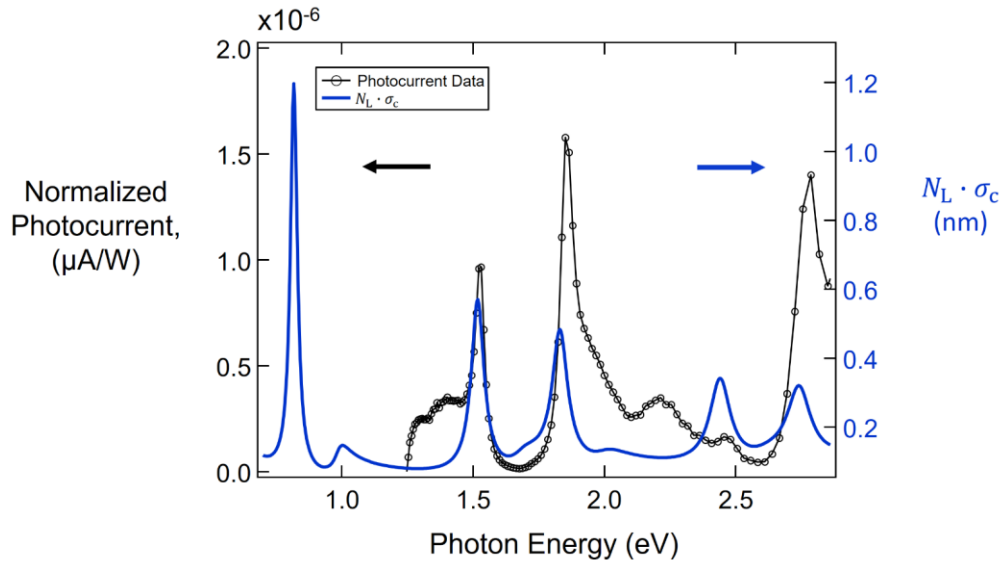


**Fig. S32** Photocurrent spectrum normalized by the laser power at the height of the nanotube 34 nm below the electrode (black) and the optical width of a (19,18) nanotube (blue).

## References

- (1) Liu, K.; Hong, X.; Choi, S.; Jin, C.; Capaz, R. B.; Kim, J.; Wang, W.; Bai, X.; Louie, S. G.; Wang, E.; et al. Systematic Determination of Absolute Absorption Cross-Section of Individual Carbon Nanotubes. *PNAS* **2014**, *111*, 7564–7569.
- (2) Perebeinos, V.; Avouris, P. Exciton Ionization, Franz–Keldysh, and Stark Effects in Carbon Nanotubes. *Nano Lett.* **2007**, *7*, 609–613.
- (3) Hertel, T.; Perebeinos, V.; Crochet, J.; Arnold, K.; Kappes, M.; Avouris, P. Intersubband Decay of 1-D Exciton Resonances in Carbon Nanotubes. *Nano Lett.* **2008**, *8*, 87–91.
- (4) Malapanis, A.; Perebeinos, V.; Sinha, D. P.; Comfort, E.; Lee, J. U. Quantum Efficiency and Capture Cross Section of First and Second Excitonic Transitions of Single-Walled Carbon Nanotubes Measured through Photoconductivity. *Nano Lett.* **2013**, *13*, 3531–3538.
- (5) Aspitarte, L.; McCulley, D. R.; Minot, E. D. Photocurrent Quantum Yield in Suspended Carbon Nanotube p–n Junctions. *Nano Lett.* **2016**, *16*, 5589–5593.
- (6) Ding, L.; Tselev, A.; Wang, J.; Yuan, D.; Chu, H.; McNicholas, T. P.; Li, Y.; Liu, J. Selective Growth of Well-Aligned Semiconducting Single-Walled Carbon Nanotubes. *Nano Lett.* **2009**, *9*, 800–805.